Mechanical Systems and Signal Processing 173 (2022) 109055

Contents lists available at ScienceDirect

Mechanical Systems and Signal Processing

journal homepage: www.elsevier.com/locate/ymssp

Error analysis and calibration of micro-vibration test platform developed for advanced pointing instrument

Xiaoxue Gong [a,d], Lin Li [b,c,*], Yang Yu [a,d,e], Li Wang [b,c], Lei Zhang [a,d,e], Miaomiao Wang [b,c], Yanpeng Wu [b,c]

[a] *Chang Guang Satellite Technology Co., Ltd., Changchun 130102, China*
[b] *Space Optoelectronic Measurement and Perception Lab., Beijing Institute of Control Engineering, Beijing 100190, China*
[c] *China Academy of Space Technology, Beijing 100094, China*
[d] *University of Chinese Academy of Sciences, Beijing 100049, China*
[e] *Changchun Institute of Optics, Fine Mechanics and Physics, Chinese Academy of Sciences, Changchun 130033, China*

ARTICLE INFO

Communicated by John E. Mottershead

Keywords:
Pointing instrument
Micro vibration
Test platform
Error analysis
Image shift

ABSTRACT

This paper builds a micro vibration test platform which is capable to obtain image shift data from an advanced pointing instrument with 1000 Hz sampling frequency and three seconds sampling time. According to the image shift error analysis, system measurement errors brought up by CCDs (Charge-Coupled Device) in form of pixel gray value skewing and those brought up by suspension apparatus locating in frequency band lower than 5 Hz, are able to be eliminated by gray value offset and high-pass filter algorithm respectively. Random measurement errors caused by electronic and mechanical noises are the main factors affecting the measurement accuracy; they obey normal distribution with standard deviation lower than 0.0116 and 0.0170 pixels respectively. The image shift measure accuracy of the test platform is calibrated better than 0.0618 pixels, which meets the demand of 0.08 pixels. The test platform is considered to work well on micro vibration impact assessment with ideal measurement accuracy.

1. Introduction

With the rapid development of spacecraft techniques on cosmic exploration, the pointing accuracy of on-board optical equipment is improving rapidly. The influence of micro vibration environment, which was not paid attention to in the past, has become into research hotspot in aerospace science and technology area [1–4]. Nowadays, the ground resolution of the earth observation satellite in LEO (Low Earth Orbit) reaches the sub-meter level, and its LOS (Line of Sight) needs to be better than one second. For the GEO (Geostationary Earth Orbit) optical satellite with the same ground resolution, the micro vibration influence on LOS needs to reach 1/70 of that of the LEO satellite, that is, milliarcsecond level. In deep space optical communication and inter-satellite communication, the pointing measurement accuracy requirement is even on the order of sub milliarcsecond [5]. Hence it is a very challenging work to build a micro vibration test platform that is capable to achieve measure data with high accuracy and evaluate affections brought up by micro vibration on optical instruments such as optical camera, optical pointing measuring instrument, and laser interferometer and so on in the ground test field [6–16].

---

[*] Corresponding author at: Space Optoelectronic Measurement and Perception Lab., Beijing Institute of Control Engineering, Beijing 100190, China.

E-mail address: cast_lilin@163.com (L. Li).

https://doi.org/10.1016/j.ymssp.2022.109055
Received 18 November 2021; Received in revised form 27 January 2022; Accepted 14 March 2022
Available online 21 March 2022
0888-3270/© 2022 Elsevier Ltd. All rights reserved.

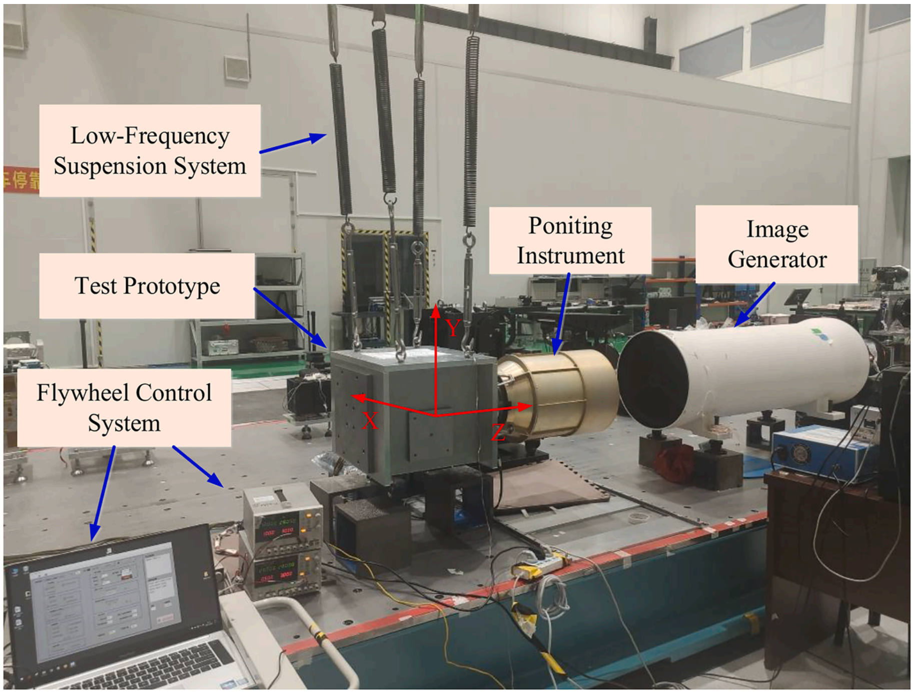

Fig. 1. Test platform overview.

Various noises in the test field are the main factors that prevent measurement accuracy of the test system further improving. The air floatation or flexible suspension device [3,6,10], which is usually used to realize the near-unconstraint environment in the process of micro vibration test, is one of the main noise sources affecting measure results. Large amounts of researches on low-frequency, low-noise air floatation and flexible suspension systems have been carried out by researchers all over the world. Rubber rope suspension method, air spring support method, near zero stiffness suspension method, and pneumatic / electromagnetic suspension technology, has been proposed for the ground micro vibration test of spacecraft [11]. Literature [12] considers that when the natural frequency of the suspension system is 1/5–1/6 or lower than the basic natural frequency of the test object, the influence of the test system can be ignored. Literature [6] and [13] provide a way to solve the low-frequency problem in the suspension system by means of flexible rope or elastic rope, and regard the suspension system as a single pendulum system, which is referential to the research of micro vibration test system. As for the suspension devices proposed in the literature [14–16], the suspension of the tested object is realized by flexible rope or elastic rope to meet the low stiffness environment requirement, and the system error and calibration were not studied. However, previous researches [17–23] mainly focus on the design and mechanical analysis of the suspension or air floatation system. Measurement error brought up by test system has not been analyzed in depth. Another important noises producer that affects test accuracy is the CCD electronic devices, related researches on affection mechanism are however, on the stage of beginning. This work realizes the calibration of noise milli-pixel level of micro vibration test system, which has not been reported in any other related research before.

The state of art of this paper is intensive studies on measurement error brought up by noises of suspension system and CCD electronic devices. Related modeling methods and error synthesis are original and haven't been proposed before. Research content of this paper is divided in to five parts. Section 2 introduces composition and principle of the test system in detail. Section 3 mainly focuses on researches of image shift error induced by CCD electronic devices. Section 4 studies the noises brought up by the suspension system composed of lifting frock and flexible spring. Based on above contents, the image shift error analysis and calibration of the whole test system is carried out in Section 5. The last section concludes the research work of this paper. The state of art of this paper will contribute to the further development of high-precision micro vibration test system and strongly support the development of spacecraft that requires 0.1″ LOS accuracy in the future.

2. Test platform

2.1. Architecture of the test platform

To measure the micro vibration impact of flywheel on pointing instrument precisely, this paper constructs a systemically test platform that can provide simulated on-orbit imaging mode as well as working environment for the study object. By speed set of flywheels assembled in the test prototype, large amounts of images can be obtained from pointing instrument to evaluate the micro vibration affection. Composition of this elaborate platform is shown in Fig. 1. Five parts including test prototype, low-frequency (LF)

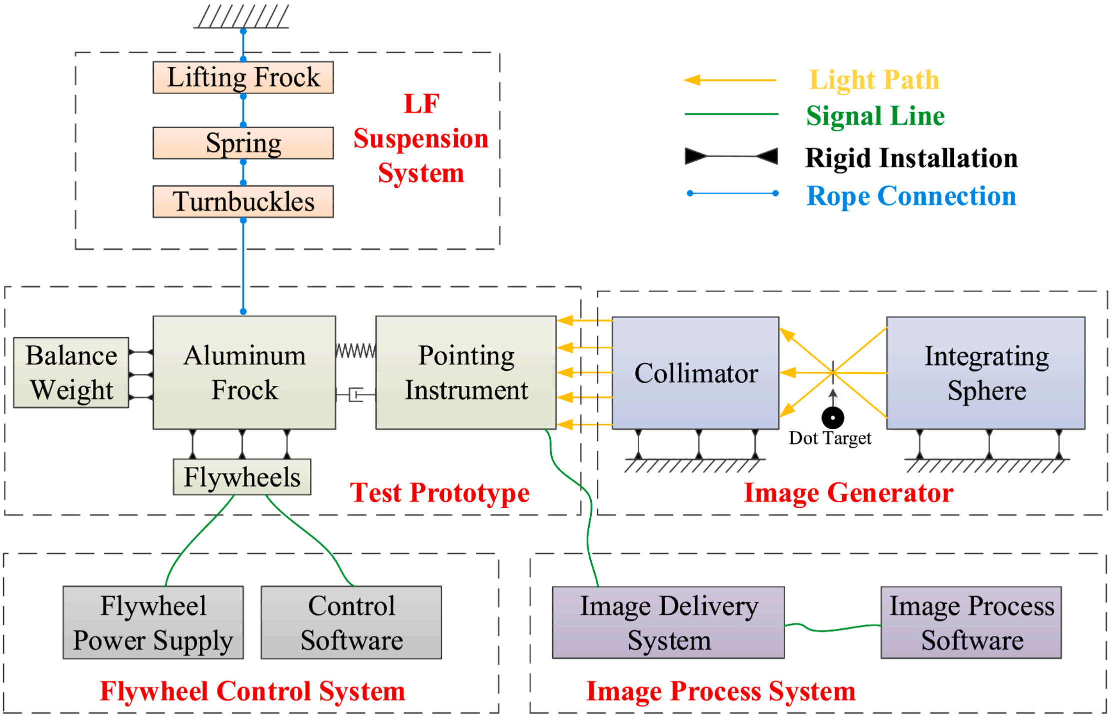

Fig. 2. Relationship between each part of the test platform.

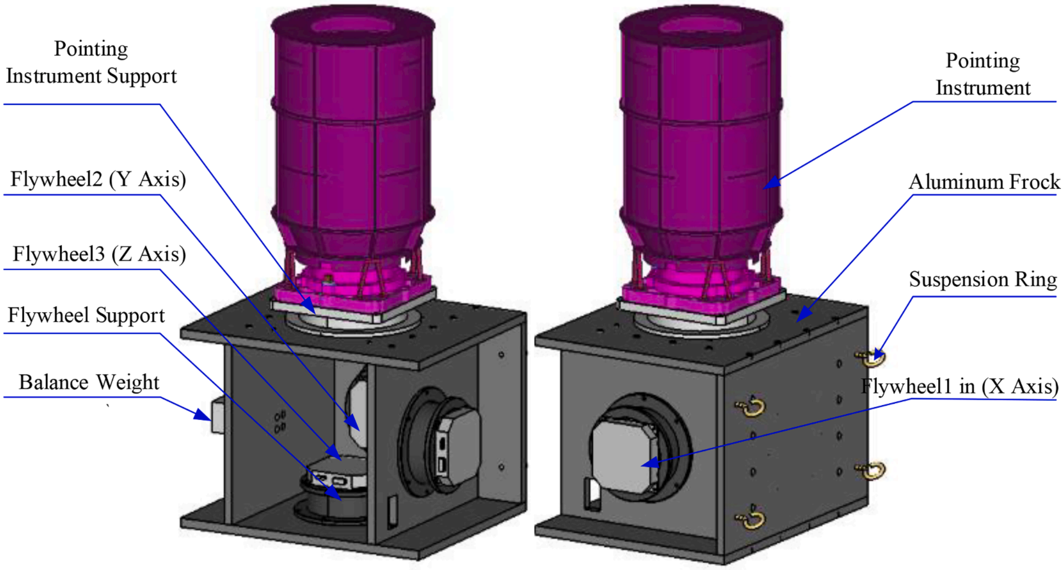

Fig. 3. Diagrammatic sketch of test prototype.

suspension system, image generator, flywheel control system and image process system (not shown in Fig. 1) participate making up the platform. Detail structure of each part and relationship between them are shown in Fig. 2.

The test prototype shown in Fig. 3 is mainly comprised of pointing instrument, aluminum frock, flywheel balance weight and corresponding support structures. The pointing instrument support and aluminum frock are carefully designed so that the constrained fundamental frequency (143 Hz) of pointing instrument agrees with launch status. The flywheel support is also well designed so that the mounting frequency of flywheel is near rigid installation and will not cause mechanical resonance with flywheels in the interest frequency spectrum (0–500 Hz). The image generator is comprised of integrating sphere, dot target and collimator, the dot target is placed at the focus in object space of collimator to simulate on-orbit parallel light input collimator (13 m focus and 0.4 m optical

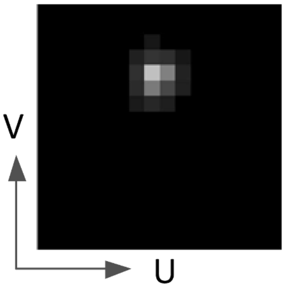

Fig. 4. A single frame image samples (16 × 16 pixels cut out).

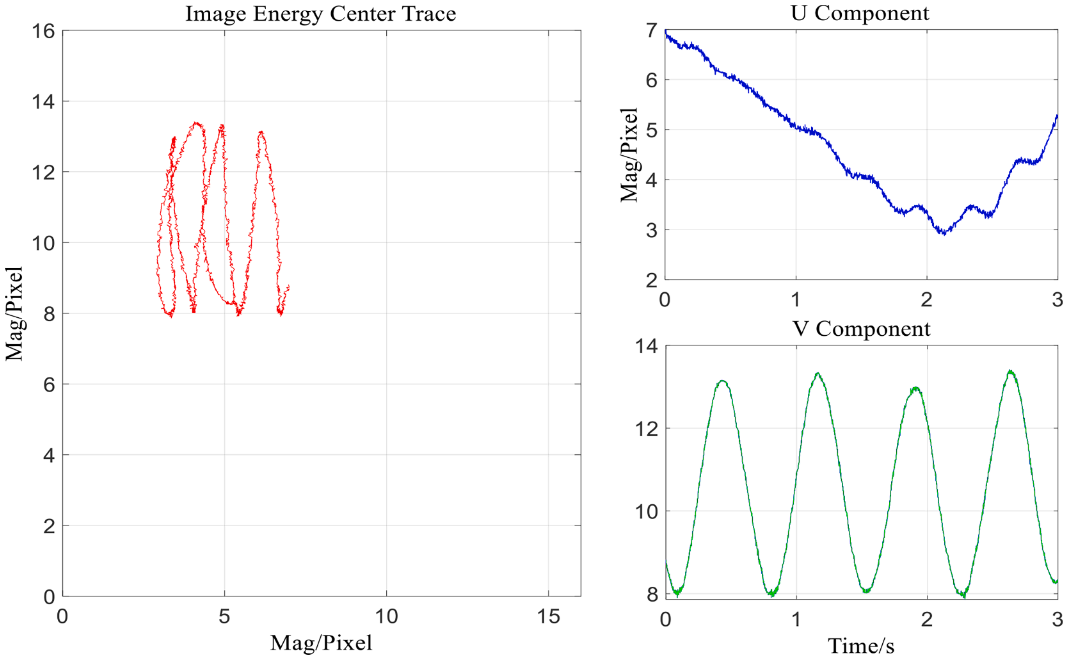

Fig. 5. Location changes of image energy center over sampling time.

aperture) and dot target (100 μm aperture) are carefully chosen so that the received images in pointing instrument have the ideal brightness and smallest diffraction. LF (Low Frequency) suspension system comprised of flexible spring, turnbuckle and lifting frock can realize pose adjustment as well as near-zero suspension frequency for test prototype. Flywheel control system is comprised of control software and flywheel power supply equipment; it is responsible for flywheel speed control and power supply. Image process system is comprised of image delivery system and process software; it is responsible for image process so as to provide valuable image data for image shift calculation.

2.2. Coordinate system

The Z coordinate is defined to be parallel to the LOS of the pointing instrument and pointing to the collimator, the Y coordinate is defined to be parallel to the gravity direction with opposite direction, the X coordinate along with Y and Z coordinates constitutes right-handed Cartesian coordinate that has been shown in Fig. 1.

2.3. Measurement process and principles

In each measurement, the test prototype is firstly hanged up by the suspension system and adjusted in front of the image generator. Then open the integrating sphere and image process system, minor adjust the turnbuckle until the pointing instrument is parallel to the collimator and images can be received in the middle field of focus plane of pointing instrument. At last, drive the flywheels by flywheel control system, images lasting 3 s are recorded by the image process system. As the sampling frequency of CCD devices mounted on the focus plane is set at 1000 Hz, total 3000 serial images are achieved in single measurement.

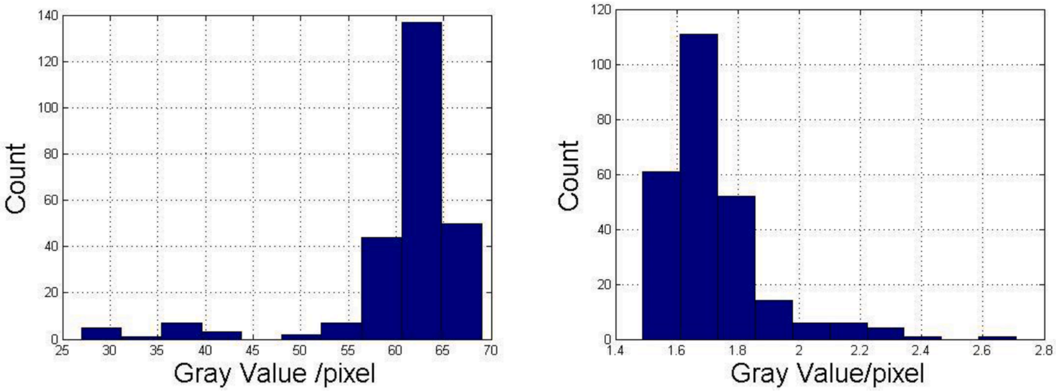

(a) Mean (b) Standard deviation

Fig. 6. Histograms of each statistical parameters.

Fig. 4 gives a single frame image sample. It can be found that received dot image has discrete boundary due to discrete sampling characteristics of CCD pixels. Image shift is selected as the output index of the test platform. Considering that brightness distribution of each discrete pixels is the same as real image, the energy center of image could be equal to image shift. The image energy center calculation formulas can be described as:

$$u_k = \frac{\sum_{j=1}^{16}\sum_{i=1}^{16} I_{ij}^k \cdot i}{\sum_{j=1}^{16}\sum_{i=1}^{16} I_{ij}^k} \tag{1}$$

$$v_k = \frac{\sum_{j=1}^{16}\sum_{i=1}^{16} I_{ij}^k \cdot j}{\sum_{j=1}^{16}\sum_{i=1}^{16} I_{ij}^k} \tag{2}$$

whereu_k,v_k stands for the energy center location of the *k-th* frame image along U and V coordinates respectively. The U-V coordinate are focus coordinate where U, V coordinates are parallel to X, Y axis shown in Fig. 1. I_{ij}^k stands for the gray value of *i-th* row, *j-th* column pixel of *k-th* frame image.

By applying Eqs. (1) and (2) on the serial images over sampling time, image energy center location changes are achieved and shown in Fig. 5.

However, Image energy center plots shown in Fig. 5 include not only information of image shift, but also information of noise responses. Noises consisting of mechanical noises induced by suspension system and electronic noises induced by CCD devices are non-negligible during the whole tests. Since 0.1″ LOS requirement are equal to 0.08-pixel image shift for the studied pointing instrument. Measurement error brought up by environmental noises should be lower than 0.08 pixels. To prove whether image shift could be derived through image energy center calculation within required error, the rest of this paper presents detail studies on analysis and calibration of the measurement error brought up by each noise.

3. Analysis and calibration of electronic noises

The image receiver assembled in the pointing instrument is an area CCD with 1000 Hz sampling frequency, it produces noises in form of pixel gray value error, including systematic gray value error determined by characteristics of each pixel and random gray value error produced by dark current, thermal noise of electronic devices. Since systematic gray value error can be easily eliminated by proper image processing algorithm, random gray value error becomes the main factor leading to measurement uncertainty of the test platform. Generally, researchers mostly achieve such uncertainty through numerical or experimental methods [24,25], and the imaging object is usually set static so that the error characteristics are stable and easier to predict. However, the imaging object of this paper is dynamic referred to the prototype, the initial location and image shape of which are unpredictable. This section promotes a theoretical method to calculate the measurement uncertainty caused by CCD random gray value error with the help of error theories.

3.1. Gray value error calibration

The gray value error of each CCD pixel is calibrated from serial image data obtained in dark test field. By statistical analysis of 3000 near-dark images over the sampling time, gray value skewing caused by system error and random error can be obtained according to the mean and standard deviation of gray value of each pixel. The histograms of each statistical parameter are given in Fig. 6.

According to Fig. 6, the gray value means of each pixel ranges from 27 to 69, all the values are recorded as an array and applied for gray value offset to eliminate systematic gray value error. Mean value of the standard deviations shown in Fig. 6(b) is 1.72, it is

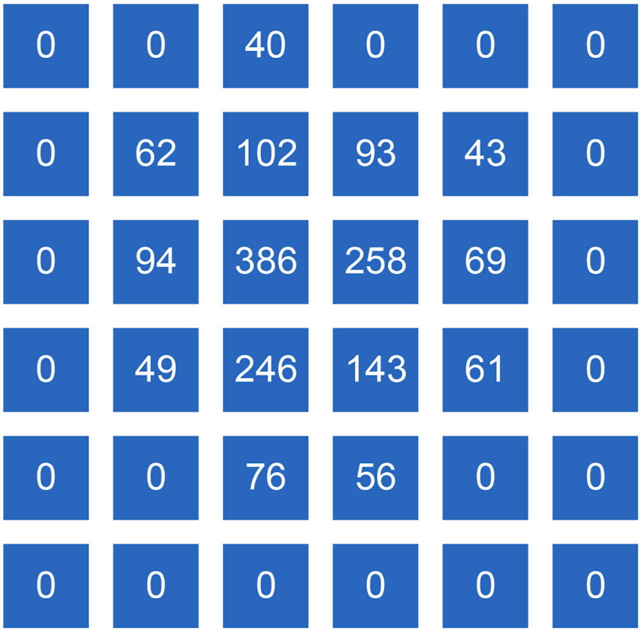

0	0	40	0	0	0
0	62	102	93	43	0
0	94	386	258	69	0
0	49	246	143	61	0
0	0	76	56	0	0
0	0	0	0	0	0

Fig. 7. Gray value of each pixel of the dot image area.

regarded as standard deviation of the normal distribution obeyed by random gray value error of each pixel.

3.2. *Error analysis for image shift calculation*

Due to the random gray value error, Eqs. (1) and (2) will bring synthetic error in image shift calculation. To reduce the synthetic error, pixel gray value is set into 0 artificially in areas whose gray value are lower than 95 percent of the brightest pixel before calculation. Fig. 7 gives the gray value of the dot image area of image sample shown in Fig. 4, it can be concluded that effective dot image area given below is smaller than 5 pixels × 4pixels. Generally, the dot image area is smaller than 6 pixels × 6pixels, the brightest area of which can reach to several hundreds. Image SNR of the darkest area of dot image can reach to an ideal value lager than 20.

Since only such 6 × 6 image cut-off has gray value after the first denoise step, pixel gray value error would only occur in these pixels. Hence synthetic error calculating equation can be described as:

$$u_k = \frac{\sum_{j=j_0}^{j_0+5}\sum_{i=i_0}^{i_0+5} I_{ij}^k \cdot i}{\sum_{j=j_0}^{j_0+5}\sum_{i=i_0}^{i_0+5} I_{ij}^k} = \mathrm{i}_0 + \frac{\sum_{j=j_0}^{j_0+5}\sum_{i=i_0+1}^{i_0+5} I_{ij}^k + \ldots + \sum_{j=j_0}^{j_0+5}\sum_{i=i_0+5}^{i_0+5} I_{ij}^k}{\sum_{j=j_0}^{j_0+5}\sum_{i=i_0}^{i_0+5} I_{ij}^k} \tag{3}$$

$$v_k = \frac{\sum_{i=i_0}^{i_0+5}\sum_{j=j_0}^{j_0+5} I_{ij}^k \cdot j}{\sum_{j=j_0}^{j_0+5}\sum_{i=i_0}^{i_0+5} I_{ij}^k} = \mathrm{j}_0 + \frac{\sum_{i=i_0}^{i_0+5}\sum_{j=j_0+1}^{j_0+5} I_{ij}^k + \ldots + \sum_{i=i_0}^{i_0+5}\sum_{j=j_0+5}^{j_0+5} I_{ij}^k}{\sum_{j=j_0}^{j_0+5}\sum_{i=i_0}^{i_0+5} I_{ij}^k} \tag{4}$$

Where, i_0 and j_0 are the first row and column of the effective image area.

Let $\delta I = 1.72$ be the standard deviation of random gray value error of each pixel, according to the standard deviation theory of arithmetic mean, we have:

$$\delta\left(\frac{\sum_{j=j_0+m}^{j_0+5}\sum_{i=i_0+n}^{i_0+5} I_{ij}}{(6-m)(6-n)}\right) = \frac{\delta I}{\sqrt{(6-m)(6-n)}} \quad (m, n \leqslant 5) \tag{5}$$

Since $\sum_{j=j_0}^{j_0+5}\sum_{i=i_0}^{i_0+5} I_{ij} >> \sum_{j=j_0}^{j_0+5}\sum_{i=i_0}^{i_0+5} \Delta I_{ij}$, the value of $\sum_{j=j_0}^{j_0+5}\sum_{i=i_0}^{i_0+5} I_{ij}$ can be regarded as a constant. According to standard deviation synthesis theory and Eqs. (3), (4) and (5), we have:

$$\delta u_k = \frac{1}{\sum_{j=j_0}^{j_0+5}\sum_{i=i_0}^{i_0+5} I_{ij}} \sqrt{30^2\delta\left(\frac{1}{30}\sum_{j=j_0}^{j_0+5}\sum_{i=i_0+1}^{i_0+5} I_{ij}\right) + \ldots + 6^2\left(\delta\frac{1}{6}\sum_{j=j_0}^{j_0+5}\sum_{i=i_0+5}^{i_0+5} I_{ij}\right)^2} = \frac{\sqrt{90}\delta I}{\sum_{j=j_0}^{j_0+5}\sum_{i=i_0}^{i_0+5} I_{ij}} \tag{6}$$

$$\delta \mathrm{v}_k = \frac{1}{\sum_{j=j_0}^{j_0+5}\sum_{i=i_0}^{i_0+5} I_{ij}} \sqrt{30^2\delta\left(\frac{1}{30}\sum_{i=i_0}^{i_0+5}\sum_{j=j_0+1}^{j_0+5} I_{ij}\right)^2 + \ldots + 6^2\delta\left(\frac{1}{6}\sum_{i=i_0}^{i_0+5}\sum_{j=j_0+5}^{j_0+5} I_{ij}\right)}^{2} = \frac{\sqrt{90}\delta I}{\sum_{j=j_0}^{j_0+5}\sum_{i=i_0}^{i_0+5} I_{ij}} \tag{7}$$

Fig. 8. Detail configuration of LF suspension system.

where δu_k, δv_k are the standard deviation of calculated image shift along U and V coordinate respectively.

According to the test data summery, the gray value sum $\sum_{j=j_0}^{j_0+5}\sum_{i=i_0}^{i_0+5} I_{ij}$ of single frame image is always larger than 1400, which leads to:

$$\delta u_k, \delta v_k \leqslant \frac{\sqrt{90}}{1400}\delta I = 0.0116 \tag{8}$$

Since noises participate the standard deviation synthesis obey normal distribution, it can be inferred that the calculated image shift also obeys normal distribution whose standard deviation is near but lower than 0.0116 pixels.

4. Analyses and calibration of mechanical noises

This paper fully considers all the mechanical noise sources, they are mass-spring system made up of test prototype and flexible springs, pendulum system made up of lifting frock, test prototype and hanging ropes, as well as complex external mechanical environment in the test field. The first two noise sources are relevant to suspension system (shown in Fig. 8), related noises are produced at low frequency spectrum with stable frequency values and large magnitudes. The last source produces noises in from of white Gaussian noise, magnitudes of which are however much smaller and obey normal distribution in broad band. Noises brought up by suspension system can be regarded as system noises, while the remaining one can be regarded as random noises.

Previous researches [17,19,23] mostly focus on the design of suspension system, the noise characteristics of the suspension system along with hanged objects are usually not studied in-depth. This paper, however, presents an intensive modeling and analysis of these mechanical noises. The suspension noises caused by flexible springs are analyzed accurately with the help of FE (Finite Element) software, while those caused by swing of test prototype are analyzed through double pendulum theories. Reasonable tests are carried out to calibrate all the mechanical noises and verify the modeling rationality. As for the mechanical random noise, it is hard to be

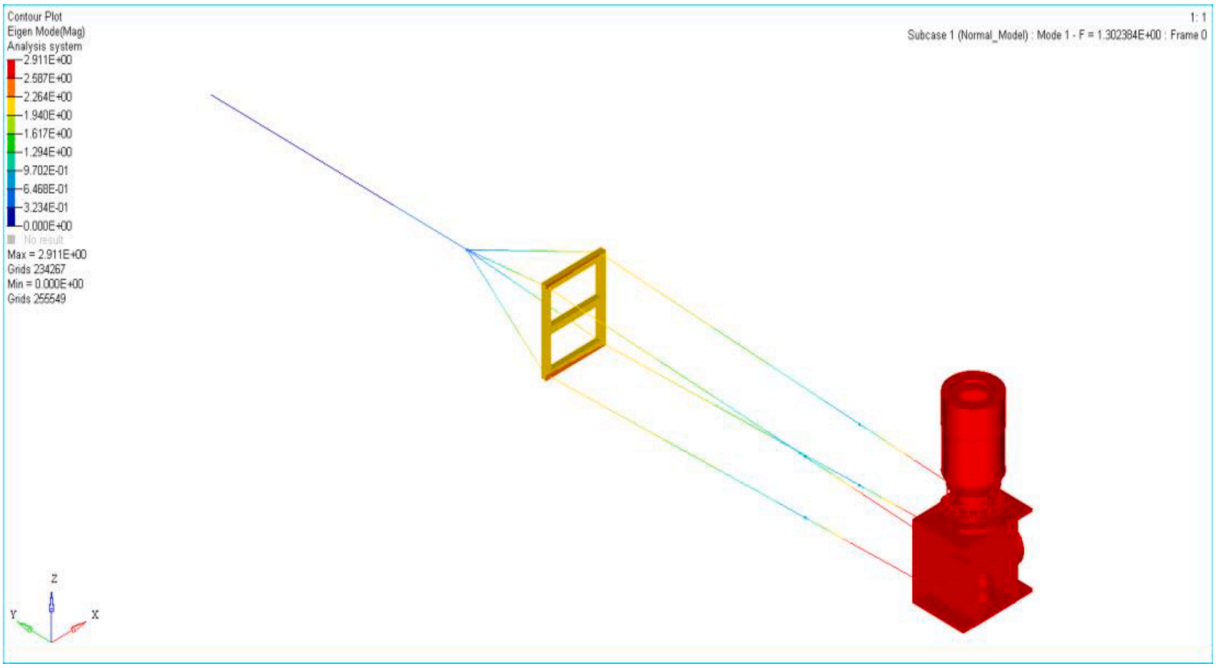

Fig. 9. The first order mode shape at 1.30 Hz.

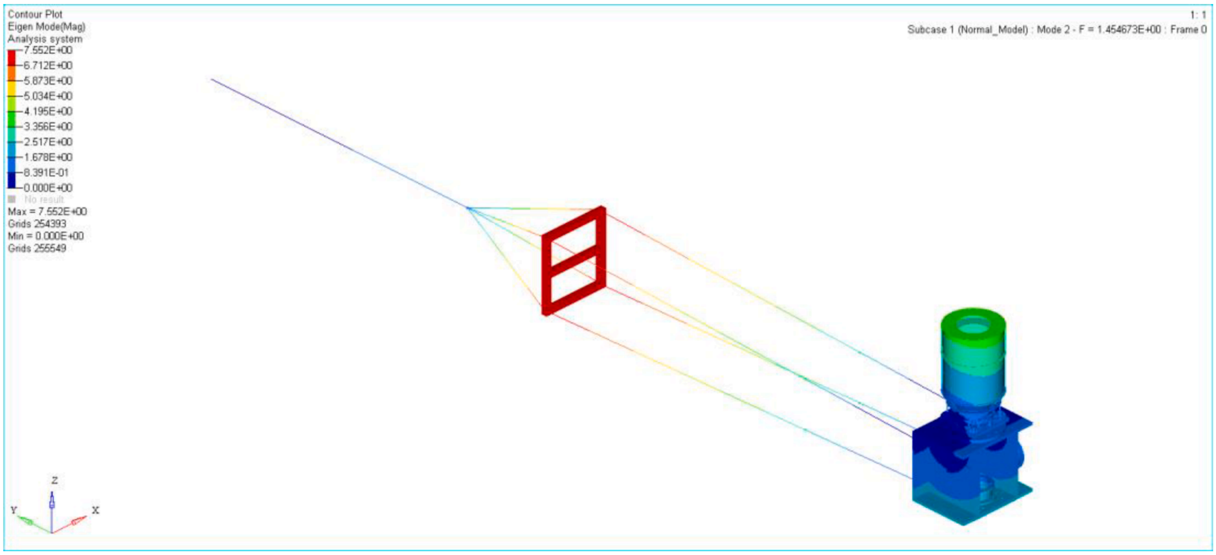

Fig. 10. The second mode shape at 1.45 Hz.

modeled by theoretical method, detail studies of which are not presented in this section, they are analyzed and calibrated in next section along with the measurement error of test platform.

4.1. Numerical simulation and analysis of suspension noises

This paper applied FEM (Finite Element Method) to analyze suspension frequency caused by flexibility of four springs; the springs are modeled as spring element in FE software. Modal analysis indicates that there exist two typical modes in this complex mass-spring system, FE model and simulation results are shown below (Fig. 9 and Fig. 10).

The first order mode shape performs periodic oscillation of test prototype along Y coordinate; it will obviously bring in image shift noise along V coordinate. The second order mode shape performs periodic rolling of test prototype about optic axis; it will bring in

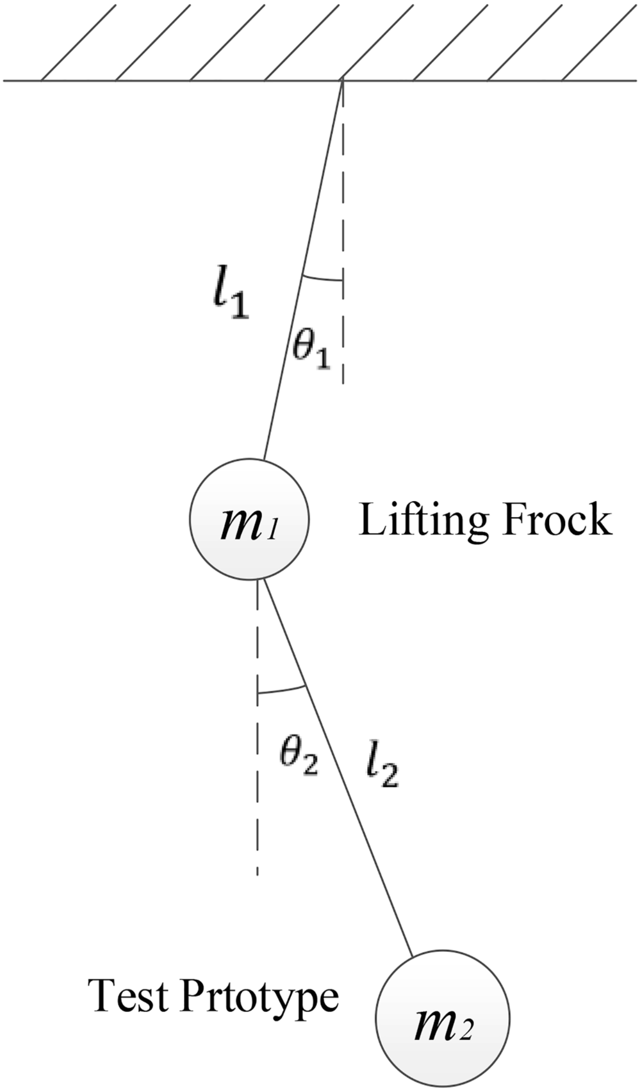

Fig. 11. Double pendulum system model diagram.

image shift noise along both U and V coordinate. However, natural frequencies of such mass-spring system are much lower than the fundamental frequency of test prototype, hence they will not impact test results that locate in high frequency spectrum, and the influences brought up by which can easily be eliminated through high-pass filter algorithm.

The suspension system can also be modeled as a double pendulum system shown in Fig. 11. Combined pendulum of lifting frock and test prototype can be modeled as equation given below:

$$\begin{cases} l_1\ddot{\theta}_1 + \dfrac{m_2}{(m_1+m_2)}l_2\ddot{\theta}_2\cos(\theta_2-\theta_1) - \dfrac{m_2}{(m_1+m_2)}l_2\ddot{\theta}_2\sin(\theta_2-\theta_1) + gsin\theta_1 = 0 \\ l_2\ddot{\theta}_2 + l_1\ddot{\theta}_1\cos(\theta_2-\theta_1) - l_1\ddot{\theta}_1\sin(\theta_2-\theta_1) + gsin\theta_2 = 0 \end{cases} \tag{9}$$

where $m_1, l_1, \theta_1, m_2, l_2, \theta_2$ are mass, rope length, rope angle for lifting frock and test prototype respectively.

Eq. (9) is a nonlinear second-order differential equation which can be solved by Runge Kutta algorithm. After Fast Fourier Transform (FFT) of the solved result, natural frequencies of the double pendulum system can be obtained and shown in Fig. 12.

It can be concluded that double pendulum system brings noises at 0.11 Hz and 0.30 Hz, according to the pendulum characteristics, image shift error brought up by which concentrate in direction of U coordinate. Since the period of pendulum noises is longer than sampling time, corresponding influence performs rigid body component in image shift along U coordinate shown in Fig. 5. Such rigid body component can be eliminated through proper image processing algorithm. The study process the image data with both polynomial fitting algorithm and high-pass filter algorithm (Chebyshev filter are selected with 1-Hz passband frequency and 0.5-Hz

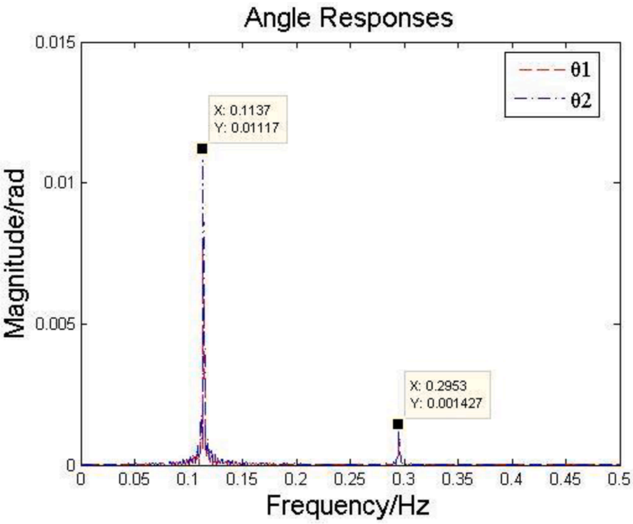

Fig. 12. Natural frequencies of the double pendulum system.

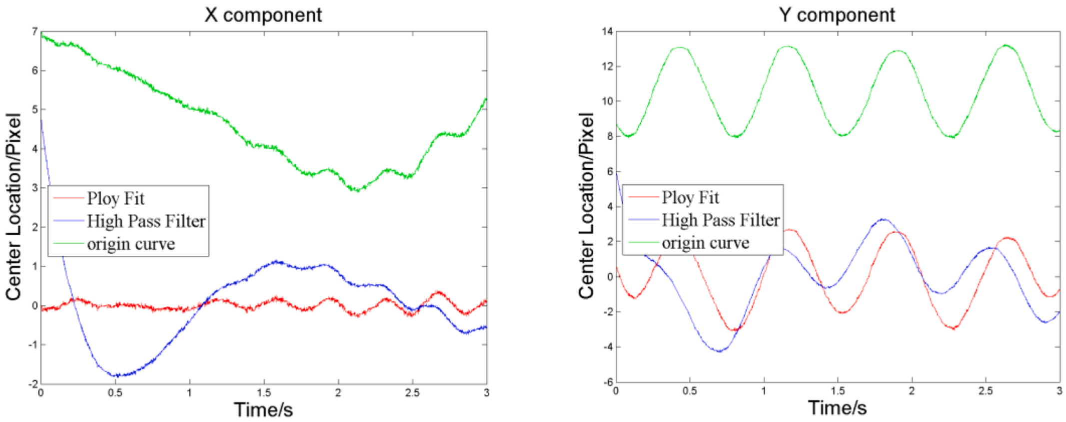

Fig. 13. Image center curves achieved by each algorithm in the time domain.

stopband frequency) to understand the differences between them, an image data (when flywheel1 working at 0 rpm) has been selected as an example to explain the advantages of polynomial fitting algorithm. The image center curves achieved by each algorithm in the time domain are shown in Fig. 13.

Since high-pass filter algorithm will bring in significant errors in transition band, the time curve results still present significant rigid body characteristics. The Image curve achieved by polynomial fitting algorithm are gentler than that achieved by high-pass filter algorithm with no extra rigid body component, so it can be concluded that that polynomial fitting algorithm are better than high-pass filter algorithm to eliminate rigid body component in image shift.

4.2. *Test and calibration of suspension noises*

According to previous analysis, Natural frequencies of suspension noises are invariant, so they can be calibrated through image data when flywheel is working at stable speed series. The flywheel1 shown in Fig. 3 is set working at stable speed ranging from 0 to 4800RPM (Revolutions Per Minute) with 300RPM increment, total 17 groups of Image data are achieved. After image energy center calculation, polynomial fitting, and FFT sequentially, the amplitude-frequency characteristics of image shift under each speed condition can be obtained and shown in Figs. 14 and 15.

Test results shows that image shift caused by structural resonance has natural frequencies much higher than those of suspension noises. It is obvious that suspension noises impact on image shift along U coordinate at 2.686 Hz–2.93 Hz while those impact on image shift along V coordinate at both 1.221–1.465 Hz and 2.686 Hz–2.93 Hz. Noise peaks locate at 1.221–1.465 Hz are more remarkable in Figs. 15 than 14, they were considered to be motivated by 1st mode shape at 1.30 Hz, hence they hardly affect image shift in U coordinate. Noise peaks locate at 2.686 Hz–2.93 Hz were considered to be motivated by the second harmonic generation of 2nd mode

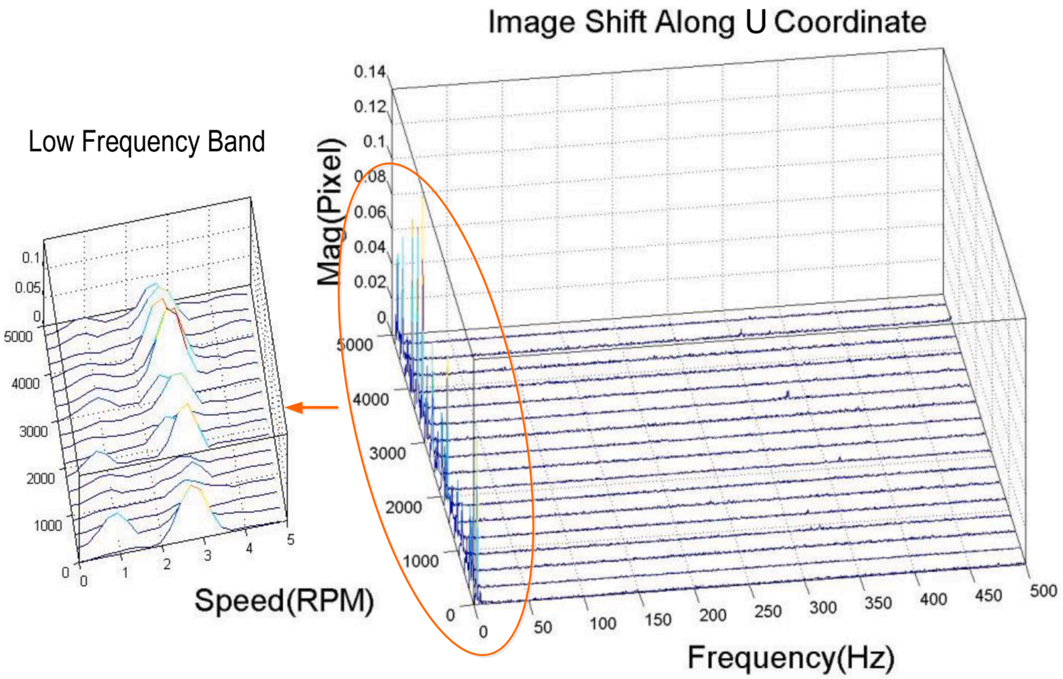

Fig. 14. Image shift along U coordinate under each speed condition.

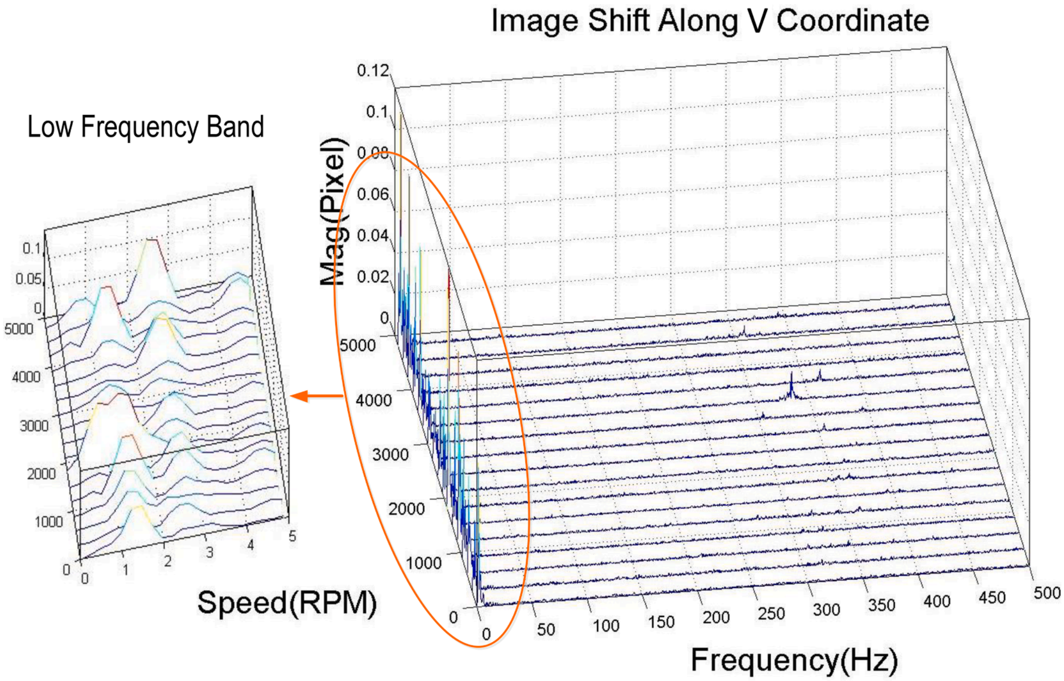

Fig. 15. Image shift along V coordinate under each speed condition.

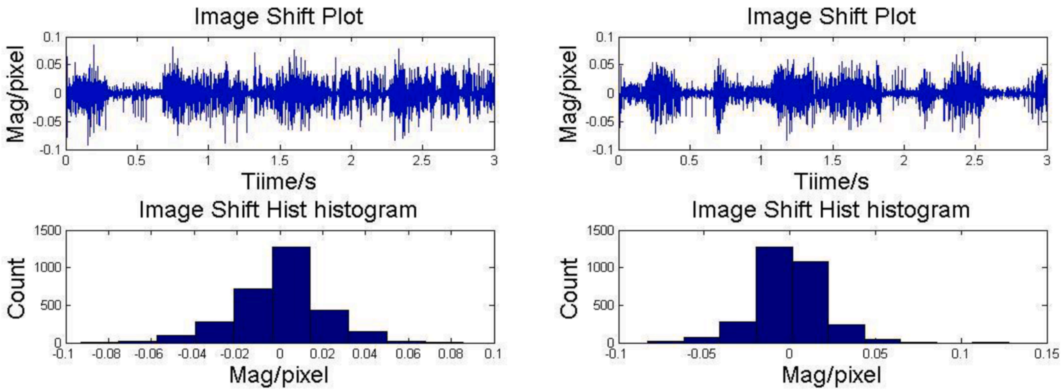

(a) Along **U** coordinate (b) Along **V** coordinate

Fig. 16. Amplitude characteristics of processed image shift data.

shape at 1.45 Hz, hence they can be observed in both Figs. 15 and 14.

5. Calibration and discussion

5.1. Calibration and analysis of test platform measurement error

Considering that system noises caused by electronic devices and suspension system can be easily eliminated through proper image process method, random noises become the main source inducing image shift measurement error. To separate their affection from that of flywheel disturbance, the authors set flywheel speed at 0 and analysis corresponding image data. After elimination of system error with image gray value offset and high-pass filter algorithm, the amplitude characteristics of processed image shift data are obtained as shown in Fig. 16.

It can be concluded from Fig. 16 that magnitudes of image shift obey normal distribution whose standard deviation is 0.0206 pixels and 0.0187 pixels along **U** and **V** coordinates respectively. According to the 3σ principle, the measurement error of image shift is lower than 0.0618 and 0.0561 along **U** and **V** coordinates respectively, which meets the measurement accuracy demand of 0.08 pixels.

Since the measurement error are mainly caused by electronic and mechanical random noises, the image shift error brought up by mechanical random noises can be calculated inversely by separating the electronic random error component from the measurement error. According to the standard deviation synthesis theory, the standard deviation of image shift error brought up by mechanical random noises can be calculated as:

$$\delta^{m}_{u,v} = \sqrt{{\delta^{s}_{x,y}}^{2} - {\delta^{e}_{x,y}}^{2}} \tag{10}$$

where $\delta^{m}_{u,v}$ and $\delta^{e}_{u,v}$ are the standard deviation of image shift error brought up by electronic and mechanical random noises respectively, $\delta^{s}_{u,v}$ is the standard deviation of image shift measurement error of the test platform.

Substitution the value of $\delta^{e}_{u,v}$ and $\delta^{s}_{u,v}$ into Eq. (10) gives:

$$\begin{cases} \delta^{m}_{u} \approx 0.0170 \\ \delta^{m}_{v} \approx 0.0147 \end{cases} \tag{11}$$

It can be known that the image shift error brought up by mechanical random noises is near 0.0170 and 0.0147 pixels along U and V coordinate respectively.

5.2. Discussion

This paper provides a detailed, in-depth and accurate way modeling and evaluating the affection brought up by all kinds of noises for an on-ground micro vibration universal test platform. The test errors brought up by each noise have been calculated and calibrated quantitatively, which strongly convinced the reasonability of the test platform. What is more worth mentioning is that the influence mechanism of different noises promoted in this paper show researches an effective way improving the accuracy of on-ground micro vibration test. The system noises are proved having little influence on the test results, so the key to improve the test accuracy is to reduce the affection of random noises such as CCD pixel gray value error and mechanical random noises. For example, the affection brought up by CCD pixel gray value error may be reduced by applying other advanced image shift calculating algorithms, however, the error synthesis for these algorithms needs be further studied.

6. Conclusions

In this paper, a ground photoelectric test platform which can measure the influence of flywheel micro vibration on image shift of the pointing instrument are carried out, the noise characteristics of which are theoretically analyzed and measured in depth. Obtained Image data indicates that there exist two main noises sources affecting the measured image shift. The CCD electronic devices bring in gray value error made up of fixed and random gray value skewing, while suspension apparatus brings in mechanical noises made up of low-frequency suspension modal responses and random environmental noises. According to intensive theoretical modeling and analysis, affections brought up by gray value error and suspension modal responses can be eliminated by gray value offset and high-pass filter algorithm, hence they have little effect on the measurement accuracy of the test platform. The rest random errors are calibrated through ingenious test sets. It is calculated that image shift error brought up by electronic random noises obeys normal distribution with standard deviation near but lower than 0.0116, those brought up by mechanical random noises also obey normal distribution with standard deviation near 0.0170 pixels and 0.0147 pixels along U and V coordinate respectively. According to the error synthesis theory and 3σ principle, the image shift measurement accuracy of the test platform built in this paper is better than 0.0618 pixels, which can satisfy the demand of evaluating flywheel disturbances impact on the imaging quality of studied pointing instrument well.

Declaration of Competing Interest

The authors declare that they have no known competing financial interests or personal relationships that could have appeared to influence the work reported in this paper.

Acknowledgements

The authors would like to thank the handling editors and anonymous reviewers for your time and effort in reviewing this paper. The authors also gratefully acknowledge the support from National Natural Science Foundation of China (No. 51905034).

References

[1] L. Li, L. Tan, L. Kong, D. Wang, H. Yang, The influence of flywheel micro-vibration on space camera and vibration suppression, Mech. Syst. Sig. Process. 100 (2018) 360–370.
[2] A. Bcy, B. Ke, 3-DoF zero power micro vibration isolation via linear matrix inequalities based on H ∞ and H 2 control approaches, Mech. Syst. Sig. Process. 153 (2) (2021) 107506.
[3] L. Li, L. Yuan, L. Wang, et al., Recent advances in precision measurement & pointing control of spacecraft, Chin. J. Aeronaut. 34 (10) (2021) 191–209.
[4] W. Xi, A. Hw, A. By, Micro-vibration suppressing using electromagnetic absorber and magnetostrictive isolator combined platform, Mech. Syst. Sig. Process. 139 (1) (2020) 106606.
[5] L. Li, L.i. Wang, L.i. Yuan, R. Zheng, Y. Wu, J. Sui, J. Zhong, Micro-vibration suppression methods and key technologies for high-precision space optical instruments, Acta Astronaut. 180 (2021) 417–428.
[6] X.X. Gong, L. Zhang, M. Xuan, Modeling and Ground-based Experimental Jitter Researches on Earth Observation Satellite, Acta Photon. Sin. 48 (03) (2019) 138–146.
[7] X. Zhang, H. Yu, Z. He, G. Huang, Y. Chen, G. Wang, A metamaterial beam with inverse nonlinearity for broadband micro-vibration attenuation, Mech. Syst. Sig. Process. 159 (2021) 107826.
[8] G. Park, D.-O. Lee, J.-H. Han, Development of multi-degree-of-freedom microvibration emulator for efficient jitter test of spacecraft, J. Intell. Mater. Syst. Struct. 25 (9) (2014) 1069–1081.
[9] S. Yi, B. Yang, G. Meng, Microvibration isolation by adaptive feedforward control with asymmetric hysteresis compensation, Mech. Syst. Sig. Process. 114 (2019) 644–657.
[10] K.C. Liu, P. Maghami, C. Blaurock, Reaction Wheel Disturbance Modeling, Jitter Analysis, and Validation Tests for Solar Dynamics Observatory[C]// Aiaa Guidance, Navig. Control Conf. Exhibit (2013).
[11] S.S. Joshi, G.W. Neat, R.D. Reasenberg, Lessons learned from multiple fidelity modeling of ground interferometer testbeds, Int. Soc. Opt. Photon. 3350 (1998) 128–138.
[12] N. Yoshida, O. Takahara, T. Kosugi, K. Ninomiya, T. Hashimoto, K. Minesugi, S. Tsuneta, K. Ichimoto, S. Shimada, Systematic Approach to Achieve Fine Pointing Requirement of SOLAR-B, IFAC Proc. 37 (6) (2004) 101–106.
[13] Y. Zhang, C. Sheng, Q. Hu, M. Li, Z. Guo, R. Qi, Dynamic analysis and control application of vibration isolation system with magnetic suspension on satellites, Aerosp. Sci. Technol. 75 (2018) 99–114.
[14] S.-B. Chen, M. Xuan, L. Zhang, S. Gu, X.-X. Gong, H.-Y. Sun, Simulating and Testing Microvibrations on an Optical Satellite Using Acceleration Sensor-Based Jitter Measurements, Sensors 19 (8) (2019) 1797.
[15] D.-O. Lee, G. Park, J.-H. Han, Experimental study on on-orbit and launch environment vibration isolation performance of a vibration isolator using bellows and viscous fluid, Aerosp. Sci. Technol. 45 (2015) 1–9.
[16] D. Addari, G. Aglietti, M. Remedia, Experimental and numerical investigation of coupled microvibration dynamics for satellite reaction wheels, J. Sound Vib. 386 (2017) 225–241.
[17] K.C. Liu, T. Kenney, P. Maghami, et al., Jitter test program and on-orbit mitigation strategies for solar dynamic observatory, NASA/CP-2007-214158[R]. NASA Goddard Space Flight Center, 2007.
[18] M.H. Liu, J. Wang, A.C. Jiao, et al., A method for simulating the free boundary condition of satellite on orbit, Spacecraft Environ. Eng. 31 (1) (2014) 19–24.
[19] C. Liu, X. Jing, S. Daley, F. Li, Recent advances in micro-vibration isolation, Mech. Syst. Sig. Process. 56-57 (2015) 55–80.
[20] L. Li, Flywheel micro-vibration mechanism and suppression integrated study for high resolution optical satellite [dissertation], University of Chinese Academy Sciences, Changchun, 2018.
[21] A. Stabile, E. Wegrzyn, G. Aglietti, Numerical and experimental validation of the breadboard model of a novel hexapod platform for high-performance micro-vibration mitigation, AIAA Scitech 2021 Forum (2021).
[22] H. Zhu, S. He, Z. Xu, et al., Iterative feedback control based on frequency response model for a six-degree-of-freedom micro-vibration platform, J. Vib. Control 1 (2021), 107754632199731.

[23] X.Z. Jia, L. Zhang, X. Zhong, et al., Testing device for affect of satellite platform micro-vibration on camera imaging. China, 105530514, [P], 20160427.

[24] S. Tang, Z. Zhou, X. Guo, et al., Improved iteration centroid algorithm based on linear CCD light-spot location[C], International Conference on Electronic Measurement & Instruments (2009) 438–440.

[25] T. Shimoda, W. Kokuyama, H. Nozato, Noise reduction of calibration system for micro-vibration measurement, Measur Sens 18 (2021) 100138.